J. Fluid Mech. (1977), *vol.* 83, *part* 1, *pp.* 1–31
Printed in Great Britain

Three-dimensional natural convection in a box: a numerical study

By G. D. MALLINSON
Department of Defence, Aeronautical Research Laboratories, Melbourne, Australia

AND G. DE VAHL DAVIS
University of New South Wales, Sydney, Australia

(Received 31 December 1975 and in revised form 8 April 1977)

The solution of the steady-state Navier–Stokes equations in three dimensions has been obtained by a numerical method for the problem of natural convection in a rectangular cavity as a result of differential side heating. In the past, this problem has generally been treated as though it were two-dimensional. The solutions explore the three-dimensional motion generated by the presence of no-slip adiabatic end walls. For $Ra = 10^4$, the three-dimensional motion is shown to be the result of the inertial interaction of the rotating flow with the stationary walls together with a contribution arising from buoyancy forces generated by longitudinal temperature gradients. The inertial effect is inversely dependent on the Prandtl number, whereas the thermal effect is nearly constant. For higher values of Ra, multiple longitudinal flows develop which are a delicate function of Ra, Pr and the cavity aspect ratios.

1. Introduction

Fluid motion in nature is three-dimensional. However, the limitations imposed by available techniques of mathematical analysis and physical experimentation have, more often than not, forced fluid dynamists to explore only those flows that are believed to be capable of approximation by a two-dimensional model. Such flows have been simulated in the laboratory in a manner which accentuates their two-dimensionality, and have been subjected to various two-dimensional methods of analysis. With the passage of time, the three-dimensionality of the real flow tends to become forgotten. The fully three-dimensional flows – those which are not capable of approximation by a two-dimensional model, and which constitute the bulk of reality – remain beyond the realms of detailed investigation.

Recently, however, several numerical methods for the solution of the three-dimensional Navier–Stokes equations have been developed. Aziz (1965), Chorin (1968), Williams (1969) and Mallinson & de Vahl Davis (1973) have described methods for the calculation of internal flows driven by buoyancy forces. Methods applicable to external flows have been presented by Hirt & Cook (1972) and Thompson, Shanks & Wu (1974). Turbulent three-dimensional flow in channels has been modelled by Deardorff (1970) and Schumann (1973); Patanker & Spalding (1972) and Patanker, Pratap & Spalding (1974, 1975) have developed a procedure for the prediction of laminar and turbulent flow fields in straight and curved pipes. Each of these methods can, within the limitations of the approximations involved, produce solutions which describe complete flows in considerable detail and therefore has the potential for providing a powerful means for exploring the three-dimensional world.

In this paper, the method described by Mallinson & de Vahl Davis (1973) has been applied to an example of buoyancy-driven flow inside a closed box subjected to differential side heating. The problem, hereafter referred to as 'the window cavity', is an abstraction of a double-glazed window, or of an insulating wall cavity, and has previously been assumed to be two-dimensional. The basic form of the flow is a recirculating roll, the axis of which is horizontal and parallel to the heated walls.

The two-dimensional flow depends on the cross-sectional height/width ratio h_z and the Rayleigh and Prandtl numbers Ra and Pr. If h_z is large, the flow in the mid-height region is nearly one-dimensional and is amenable to theoretical analysis. Batchelor (1954) obtained a series solution applicable to weak flow when conduction is the predominant mode of heat transfer ($Ra \leqslant 10^3$). Boundary-layer models were postulated by Batchelor (1954) and Gill (1966) for higher Ra, convection-dominated flows. Near $Ra = 10^5$, the flow becomes unstable; this results in the generation of secondary rolls embedded in the low Rayleigh number single-roll base flow. This instability has been the subject of linear stability analysis: Gershuni (1953), Vest & Arpaci (1969) and Gill & Davey (1969), for example, have estimated the conditions leading to secondary motion and the wavelength of the motion at the onset of instability.

Many numerical studies of this problem have been made. For a given number of mesh points, the greatest accuracy is achieved if the solution domain is a cube, or in the case of a two-dimensional model, a square. The case $h_z = 1$ was therefore included in the initial numerical investigations conducted by Poots (1958), Wilkes & Churchill (1966), Elder (1966) and de Vahl Davis (1968). As computing methods and machinery have improved, an increasing number of solutions have been published with $h_z \gg 1$ (e.g. Rubel & Landis 1969; Thomas & de Vahl Davis 1970; de Vahl Davis & Mallinson 1975). Numerical two-dimensional solutions have now covered the conduction and boundary-layer regimes up to the onset of temporal instability in the vicinity of $Ra = 10^7$. Recently, Cormack, Leal & Seinfeld (1974) and Cormack, Leal & Imberger (1974) have presented numerical and analytical solutions respectively for the case $h_z \ll 1$, which is relevant to the prediction of the dispersion of pollutants and heat waste in estuaries.

Experimental investigations, of which Brooks & Probert (1972) provide a summary, implicitly assume that the flow field is two-dimensional. Invariably, the isothermal walls are opaque and hinder the observation of three-dimensional flows while the integrating nature of optical methods for detecting the temperature field precludes three-dimensional sensitivity. As a result, virtually nothing is known of the form or significance of the three-dimensional effects which *must* occur in a real, or experimental, cavity.

The validity of the two-dimensional assumption and the form and significance of any three-dimensional effects that may in fact occur are the subjects of this investigation.

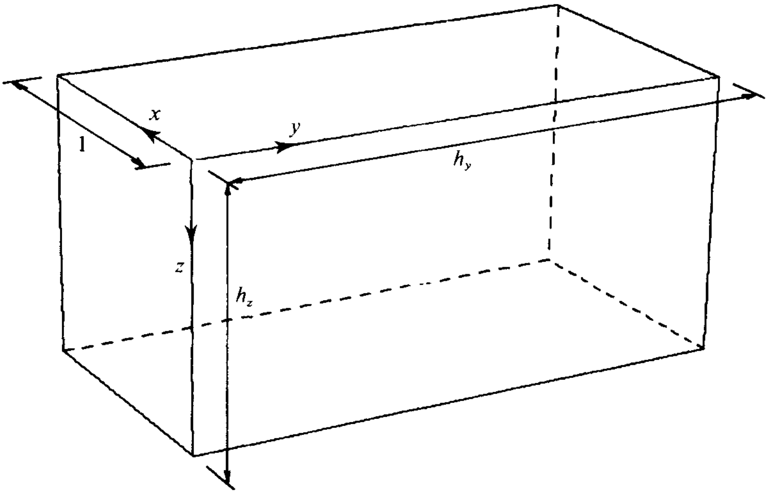

FIGURE 1. Cavity dimensions and orientation.

2. Mathematical formulation and solution method

The box, a rectangular parallelepiped, is assumed to be filled with a viscous heat-conducting fluid, and the conditions are such that the familiar Boussinesq (1903) approximations may be made. The origin of a rectangular Cartesian co-ordinate system is placed at an upper corner of the box and the axes are orientated as illustrated in figure 1. Choosing L, the size of the box in the x direction, as the scale factor for length, the shape of the box is determined by the non-dimensional aspect ratios h_y and h_z. The use of L^2/κ, κ/L and $\rho_0\kappa^2/L^2$ (where κ is the coefficient of thermal diffusivity and ρ_0 the density of the fluid at a reference temperature T_0) as scale factors for time, velocity and pressure, and the introduction of $\theta = (T-T_c)/(T_h-T_c)$ (where T is the local temperature of the fluid and T_h and T_c are the temperatures of the hot and cold boundaries) permit the equations representing the conservation of momentum, mass and energy for steady motion to be written as

$$(\nabla\times\mathbf{v})\times\mathbf{v} = -\nabla p - Ra\,Pr\,\theta\mathbf{k} + Pr\,\nabla^2\mathbf{v}, \tag{1}$$

$$\nabla.\mathbf{v} = 0, \quad \nabla.(\mathbf{v}\theta) = \nabla^2\theta. \qquad (2), (3)$$

The velocity vector has been denoted by $\mathbf{v} = u\mathbf{i}+v\mathbf{j}+w\mathbf{k}$ (where $\mathbf{i}$, $\mathbf{j}$, $\mathbf{k}$ are unit vectors in the x, y and z directions respectively); p is the perturbation of the total pressure from the first-order hydrostatic value; $Ra = g\beta(T_h-T_c)\,L^3/\kappa\nu$ and $Pr = \nu/\kappa$ are the Rayleigh and Prandtl numbers, where β and ν are respectively the coefficients of volumetric expansion and kinematic viscosity and g is the gravitational acceleration (the direction of which is parallel to $\mathbf{k}$).

It is convenient to recast the governing equations in terms of $\boldsymbol{\zeta} = \zeta_1\mathbf{i}+\zeta_2\mathbf{j}+\zeta_3\mathbf{k}$, the vorticity vector, and a vector $\boldsymbol{\psi} = \psi_1\mathbf{i}+\psi_2\mathbf{j}+\psi_3\mathbf{k}$, which is a solenoidal potential for $\mathbf{v}$. Equations (1) and (2) are then replaced by

$$Pr^{-1}[\nabla\times(\boldsymbol{\zeta}\times\mathbf{v})] = -Ra\,(\nabla\times\theta\mathbf{k})+\nabla^2\boldsymbol{\zeta} \tag{4}$$

and

$$\boldsymbol{\zeta} = -\nabla^2\boldsymbol{\psi}. \tag{5}$$

The boundaries at $x = 0$ and $x = 1$ are assumed to be isothermal and held at constant temperatures T_c and T_h respectively. All other boundaries are assumed to be adiabatic.

The boundary conditions for $\boldsymbol{\psi}$ and $\boldsymbol{\zeta}$ are derived from the velocity boundary conditions. Each boundary is assumed to be impermeable and at rest. As explained by Hirasaki & Hellums (1968), the condition of impermeability implies that $\boldsymbol{\psi}$ is normal to the boundary and that the normal derivative of its normal component is zero; i.e. at $x = 0$, for example,

$$\partial\psi_1/\partial x = \psi_2 = \psi_3 = 0. \tag{6}$$

The no-slip condition at the stationary boundaries, together with (6), implies conditions on $\boldsymbol{\zeta}$ exemplified by

$$\zeta_1 = 0, \tag{7}$$

$$\zeta_2 = -\partial^2\psi_2/\partial x^2, \quad \zeta_3 = -\partial^2\psi_3/\partial x^2 \tag{8}$$

on $x = 0$.

Equations (6) are used as boundary conditions for the solution of (5) for $\boldsymbol{\psi}$, while (7) and, after suitable integration, (8) are used as boundary conditions for the solution of (4) for $\boldsymbol{\zeta}$.

The window cavity exhibits symmetry about the plane $y = \frac{1}{2}h_y$. It is necessary, therefore, to obtain solutions over only one half of the cavity. The plane $y = \frac{1}{2}h_y$ is adiabatic; (6) still apply; and (7) and (8) are replaced by $\zeta_1 = \zeta_3 = 0$ and $\partial\zeta_2/\partial y = 0$ at $y = \frac{1}{2}h_y$.

Complete details of the component partial differential equations comprising the system (1), (4) and (5), the vector-potential boundary conditions and the numerical solution method were presented by Mallinson & de Vahl Davis (1973). Briefly, the method relies on approaching the steady solution of (3)–(5) via a false transient defined by

$$\alpha_\zeta^{-1}\partial\boldsymbol{\zeta}/\partial t = Pr^{-1}\nabla\times(\boldsymbol{\zeta}\times\mathbf{v}) - Ra(\nabla\times\theta\mathbf{k}) + \nabla^2\boldsymbol{\zeta}, \tag{9}$$

$$\partial\boldsymbol{\psi}/\partial t = \nabla^2\boldsymbol{\psi} + \boldsymbol{\zeta}, \quad \partial\theta/\partial t = -\nabla.(\mathbf{v}\theta) + \nabla^2\theta. \tag{10), (11}$$

A set of finite-difference equations is generated by replacing the derivative terms in (9)–(11) and in the boundary conditions by second-order central-difference approximations. The iterative solution procedure is essentially an alternating direction implicit approximation to the above set of parabolic equations. The parameter α_ζ and the magnitude of the time step δt may be selected to enhance the approach to a steady state. All the solutions presented herein were obtained with $\alpha_\zeta = 0{\cdot}05$ and $\delta t = 2\delta x^2$ (where δx is the smallest mesh interval).

Results have been obtained for a reasonably wide range of parameter values. With the assumption of symmetry about the $y = \frac{1}{2}h_y$ plane, a cubical solution domain (which yields the greatest accuracy for a given number of mesh points) corresponds to a cavity with $h_y = 2$ and $h_z = 1$. The present investigation was begun by obtaining a series of solutions with these aspect ratios, with $Pr = 1$ and with Ra increasing up to $1{\cdot}5\times10^5$. These solutions were later augmented by a similar series with $Pr = 0{\cdot}71$ and $10^4 \leqslant Ra \leqslant 10^6$ so that the results were applicable to air-filled cavities. Isolated solutions with different values of h_y, h_z and Pr extended the range of the investigation to a region broadly defined by $0 \leqslant Ra \leqslant 10^6$, $0{\cdot}1 \leqslant Pr \leqslant 100$, $1 \leqslant h_y \leqslant 5$ and $1 \leqslant h_z \leqslant 5$. The case $h_y = 5$ and $h_z = 5$ was included to provide the closest approximation to a real window cavity that could be achieved within the limitations imposed by the available computing equipment.

These limitations are felt in terms of the maximum resolution that can be achieved by the finite-difference mesh. The solutions presented in this paper were computed on an IBM 360/50 and on a PDP-10: on each machine the practical upper limit to the number of mesh points was approximately 6000. Consequently, the majority of solutions were obtained with a $15 \times 15 \times 15$ mesh, which was considered to represent a reasonable compromise between accuracy and computing cost, bearing in mind the fact that the exploratory nature of the investigation demanded a larger number of solutions rather than extreme accuracy. Naturally, the number of mesh points was increased in cases where better resolution was necessary (such as a cavity with large h_y or h_z). Each solution was obtained after approximately 100 iterations, which required about 30 min of central processor time on the PDP-10 or approximately 50 min on the IBM 360/50.

The accuracy of the solutions is, of course, of considerable importance. Unfortunately, because of their demands on computer storage and time, it was not practicable to explore the effects on the truncation errors of further mesh refinement in the three-dimensional solutions.

Some two-dimensional solutions were obtained using 15×15 and 51×51 meshes. It is more convenient to discuss the quantitative results below, but it may be noted here that in no case did the *form* of the solution (including some quite complex features) change with the mesh size. Quantitative results are of declining quality with increasing *Ra*, but the quantitative solutions are reliable in all cases.

3. Solution display methods

In the case of a two-dimensional steady flow, the streamlines correspond to lines of constant stream function and a single contour map can give a complete portrayal of the flow field. For a three-dimensional flow a similar presentation is not possible. The description of a three-dimensional vector field in terms of two-dimensional diagrams is not easy. Moreover, the relationship between $\boldsymbol{\psi}$ and the streamlines is much more complicated than for two-dimensional flow.

Each solution is determined by four fields, namely ψ_1, ψ_2, ψ_3 and θ. In addition, the components of $\mathbf{v}$ and $\boldsymbol{\zeta}$ can be derived from $\boldsymbol{\psi}$, making a total of ten fields of numerical data from which features of the flow can be deduced.

One approach to the display of the data is to take plane slices of the field and construct contour maps of the variation over each slice of the solution variables (e.g. Aziz 1965). However, this technique is really only successful in the description of scalar quantities such as θ and it is extremely difficult to construct a complete image of a vector field from a sequence of plane-slice contour maps of each of its components. Even in the description of a scalar, the presentation is hindered by the large number of contour maps that are usually generated.

In this paper, contour maps are used solely for the display of scalar fields. Each map is drawn as if the slice has been viewed by looking in the positive direction of the coordinate axis normal to the slice.

The field lines of a vector field are fundamental to the description of that field. For example, the field lines of the velocity field are the streamlines, which in the case of steady flow are identical to particle tracks. Holst & Aziz (1972) computed particle tracks from their three-dimensional solutions for transient natural convection in a porous medium but presented the results only in terms of two-dimensional elevations. During the present investigation, their method was improved and a perspective projection incorporated to provide a particularly effective method for the interpretation of three-dimensional solutions.

The components of the vector potential at any point on a particle track are obtained by interpolation from the values at the surrounding mesh points. The velocity components are found from $\nabla \times \boldsymbol{\psi}$, and increments in the particle position are obtained by integration using a fourth-order Runge–Kutta method described in detail by Romanelli (1960). His algorithm, which is an adaptation of a method described by Gill (1951), has been optimized with respect to computational efficiency and incorporates a corrective procedure designed to minimize the accumulation of round-off errors.

Typically, the time step for the integration was so chosen that the maximum distance moved during each step was less than one-tenth of a mesh interval. The error incurred at each step (using 8 figure calculations) was estimated to be $O(10^{-6})$ relative to the width of the cavity in the x direction.

Although described in terms of the use of the velocity field for the construction of streamlines, the procedure can be used for the construction of the field lines of any solenoidal vector field. In particular, since $\nabla . \boldsymbol{\zeta} = 0$ and $\boldsymbol{\zeta} = \nabla \times \mathbf{v}$, vortex lines can readily be traced by replacing $\boldsymbol{\psi}$ and $\mathbf{v}$ by $\mathbf{v}$ and $\boldsymbol{\zeta}$ respectively.

The field lines presented in §4 are the end result of an exploratory process which involves the use of an interactive graphics display terminal connected to the computer in which the field-line calculations are performed. It is not possible to generate automatically a set of field lines that will describe an entire flow field. Instead, each solution must be explored laboriously to select the most suitable field lines and then the most appropriate viewpoint. A considerable amount of computer time is required before each solution is thoroughly investigated, and in fact the exploration of each solution typically required of the order of three times the computer time used to generate the solution!

By updating the picture on the display after each increment of the line has been computed, the viewer is presented with a moving image of the growth of the line. In the case of streamlines, growing in constant time steps, the image sequence represents the movement of a fluid element. By photographing each image, this moving sequence can be recorded and a particularly striking feature of the resulting movie film is the representation of the velocity of the element. A continuous change of viewpoint with the track length held constant can result in an effective method of resolving ambiguity in the perspective transformation. A 16 mm film† *Computer Simulation of Three-Dimensional Flow* has been made which illustrates the effectiveness of this display medium in enhancing the interpretation of three-dimensional numerical solutions.

---

† Available on loan from the authors.

4. Discussion of results

4.1. *Two-dimensional flow*

Before describing the three-dimensional solutions, it is necessary to consider the relevant two-dimensional predictions of the cross-sectional flow, as the three-dimensional end effects will depend significantly on the form of the flow far from each end wall. The two-dimensional model is in fact equivalent to a three-dimensional model with perfect-slip adiabatic boundaries at $y = 0$ and $y = h_y$ and it is convenient for the interpretation of the three-dimensional solutions to regard the two-dimensional solutions in this light. The conventional scalar velocity and stream function then correspond to the y components of $\boldsymbol{\zeta}$ and $\boldsymbol{\psi}$ respectively.

For a cavity with $h_z = 1$, Elder (1965*b*) observed two secondary rolls at

$$Ra = 9{\cdot}6 \times 10^6$$

in a cavity filled with water ($Pr = 7{\cdot}14$). Similar rolls were observed by de Vahl Davis (1968) in a numerical solution for the same aspect ratio and the conditions

$$Ra = 1{\cdot}5 \times 10^5$$

and $Pr = 10^3$ and are also evident in solutions published by Fromm (1971) for $Ra = 10^5$ and $Pr = 1$, by Quon (1972) for $Ra = 8 \times 10^5$ and $Pr = 7{\cdot}14$ and by Cormack, Leal & Seinfeld (1974) for $Ra = 1{\cdot}4 \times 10^5$ and $Pr = 6{\cdot}983$.

In a square cavity, the secondary rolls do not result from an instability of the base flow but are a direct consequence of the convective distortion of the temperature field. The flow may be regarded as being driven by the generation of vorticity by horizontal temperature gradients. Positive y vorticity, which leads to clockwise rotation when viewed by looking in the $+y$ direction, is generated by positive $\partial\theta/\partial x$. For $Ra \leqslant 10^4$, $\partial\theta/\partial x$ is positive over the whole interior region of the cross-section. Negative vorticity is produced within the viscous boundary layers and the ultimate form of the steady flow is determined by the transport balance governed by the y component of (4). As Ra increases, the development of thermal boundary layers intensifies $\partial\theta/\partial x$ in the vicinity of the walls, and the convection within each layer leads to negative $\partial\theta/\partial x$ in the centre of the cross-section. A vorticity sink thus separates the regions of concentrated vorticity generation, and, provided that viscous diffusion does not completely smear the distribution of vorticity, two secondary rolls are formed.

Two-dimensional solutions obtained during the initial phases of this investigation indicate that reversed temperature gradients appear in square cavities if

$$Ra \geqslant 3 \times 10^4, \quad \text{for} \quad 0{\cdot}1 \leqslant Pr \leqslant 100.$$

However, viscous diffusion retards the developments of secondary rolls until

$$Ra \geqslant 6 \times 10^4.$$

The solution for $Ra = 1{\cdot}5 \times 10^5$ and $Pr = 100$, illustrated in figures 2(*a*) and (*b*), exhibits these rolls. They are sufficiently strong to convect the temperature field to the extent that the isotherms are nearly horizontal in the centre of the cross-section. Note that the roll centres are on the same side of the horizontal centre-line as the regions of

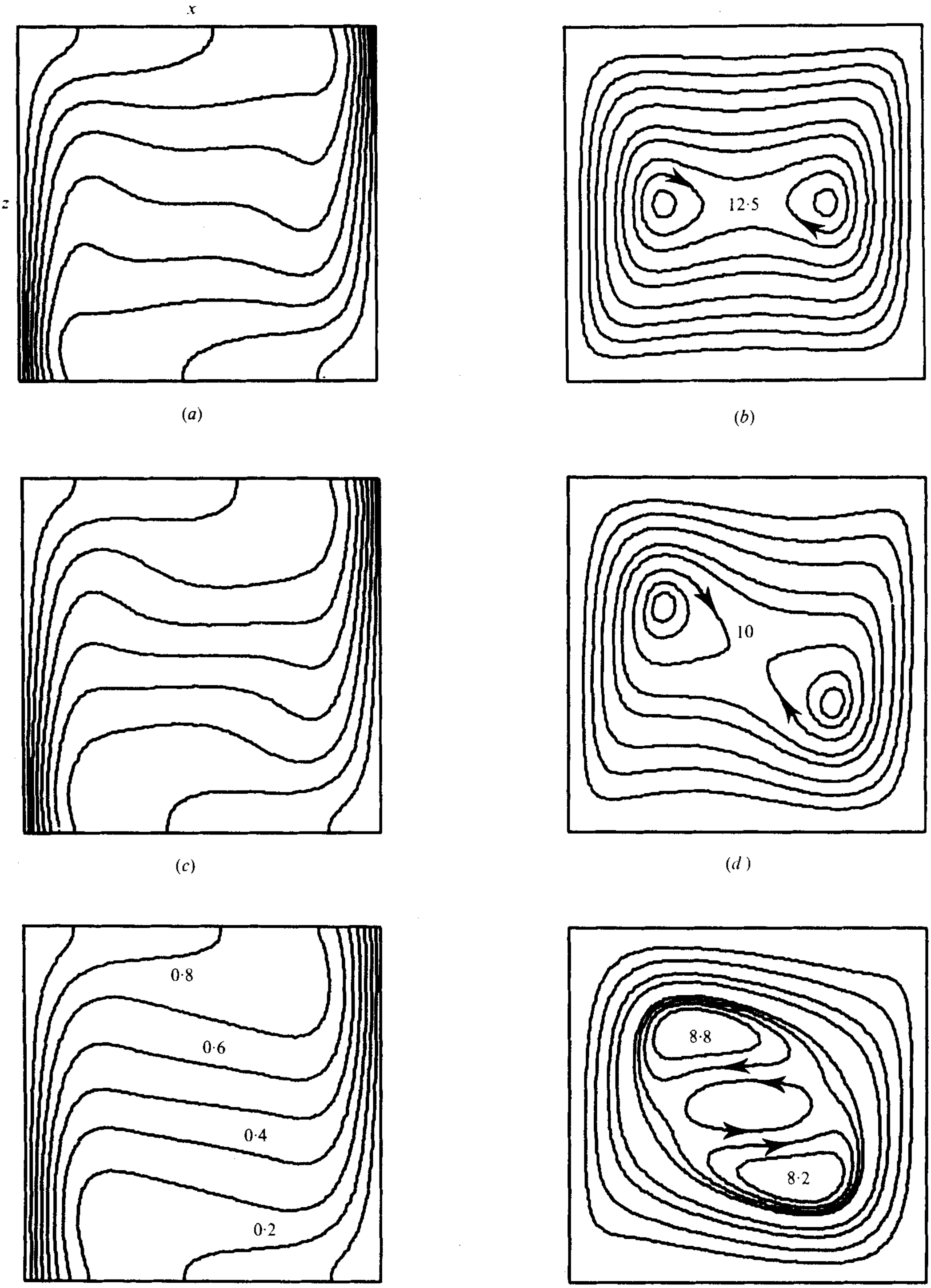

(*a*) (*b*)

(*c*) (*d*)

(*e*) (*f*)

FIGURE 2. Two-dimensional temperature (*a*, *c* and *e*) and stream-function (*b*, *d* and *f*) fields for $Ra = 1{\cdot}5 \times 10^5$ and $Pr = 100$ (*a* and *b*), $Pr = 0{\cdot}71$ (*c* and *d*) and $Pr = 0{\cdot}2$ (*e* and *f*). Contour levels for θ are 0·1 (0·1) 0·9. Contour levels for ψ are (*b*) 2 (2) 10, 11, 12, 12·5, 12·8, (*d*) 2 (2) 8, 9, 10, 10·5, 10·7, (*f*) 2 (2) 6, 7, 8·2, 8·4, 8·6, 8·8.

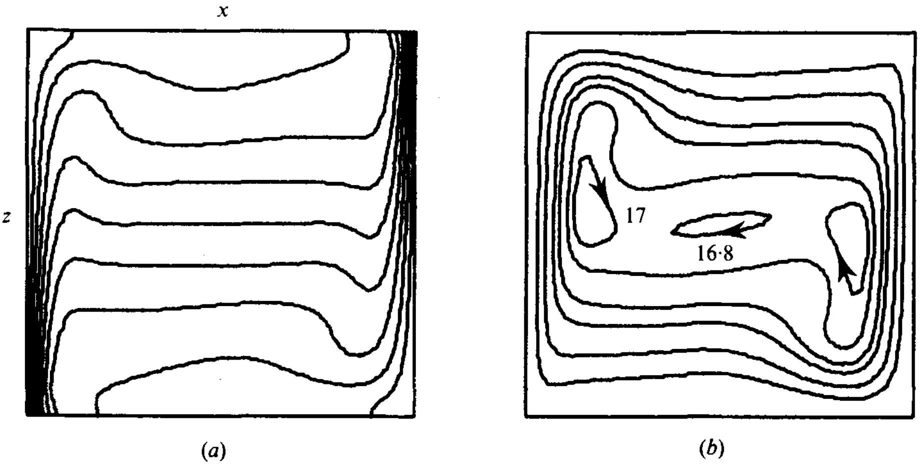

FIGURE 3. Two-dimensional (*a*) temperature and (*b*) stream-function field for $Ra = 10^6$ and $Pr = 0{\cdot}71$. Contour levels for θ are 0·1 (0·1) 0·9 and for ψ are 4, 8 (2) 16, 16·8, 17.

large positive $\partial\theta/\partial x$ (figure 2*a*). This contrasts with the flow at $Ra = 1{\cdot}5\times10^5$ and $Pr = 0{\cdot}71$, illustrated in figures 2(c) and (*d*), in which the roll centres have been displaced as a result of the increased convection of vorticity at the lower value of Pr. This observation is also supported by the numerical solutions of de Vahl Davis (1968) for $Ra = 1{\cdot}5\times10^5$ and $Pr = 100$ and Fromm (1971) for $Ra = 10^5$ and $Pr = 1$. It is interesting that this change in flow form with Pr occurs with very little change in the temperature field and hence in the rate of heat transfer, as reported by de Vahl Davis (1968).

As Pr is further decreased, the distortion of the secondary rolls increases and their effect on the temperature field diminishes. Eventually the vorticity sink at the centre of the cross-section is strong enough to support the existence of a distinct, counter-rotating roll as shown in figures 2(*e*) and (*f*) for $Ra = 1{\cdot}5\times10^5$ and $Pr = 0{\cdot}2$. The fact that this roll is buoyancy-driven, rather than arising from shear between the two outer rolls, is evidenced by the fact that the greater shear but much smaller $\partial\theta/\partial x$ which exist under the conditions of figures 2(*b*) and (*d*) do *not* generate such a roll.

With increasing Ra, the secondary rolls intensify and their centres move towards the side walls. In the case of a high Pr fluid the secondary motion persists as two rolls up to the onset of temporal instability as may also be seen in Quon's (1972) solution and Elder's (1965*b*) experiment. For $Pr = 0{\cdot}2$, the present solutions indicate that the three-roll system of figure 2(*f*) persists. However for unit-order Pr an intriguing phenomenon occurs which is illustrated by the solution for $Ra = 10^6$ and $Pr = 0{\cdot}71$ in figures 3(*a*) and (*b*). A central secondary roll exists which, unlike that in the low Pr flow, rotates in the *same* direction as the base flow. Examination of the solution from which the isotherms in figure 3(*a*) were prepared reveals that $\partial\theta/\partial x$ is small but *positive* in the centre of the cross-section (as a result of the convective effect of the flow in the secondary rolls), leading to the generation of clockwise (i.e. positive) vorticity in this region. The gradient is very weak and the roll does not exist at higher values of Pr, when viscous diffusion is greater. For $Ra \geqslant 3\times10^5$, the roll was observed for $0{\cdot}71 \leqslant Pr \leqslant 1$.

In cavities with $h_z \gg 1$, it is well established that, when Ra exceeds a critical value, a vertical series of secondary rolls develops as a result of instability of the base flow with respect to disturbances that are periodic in z. The experiments of Elder (1965*a*) and the numerical solutions of de Vahl Davis & Mallinson (1975) suggest that this is true if $h_z \geqslant 10$. Rubel & Landis (1969) published solutions for $h_z = 5$ which exhibit secondary rolls that bear a marked resemblance to those occurring in a square cavity. Thus for $h_z \leqslant 5$, the secondary motion is driven by buoyancy effects arising from the distortion of the temperature field by the flow, while, for $h_z \geqslant 10$, the secondary motion is the result of physical instability. Unfortunately, the three-dimensional solutions do not cover this interesting aspect of convection in a window cavity. For reasons that will be discussed later, solutions for $h_y = 5$ could be obtained only for $Ra \leqslant 3 \times 10^4$, which is considerably below the value of Ra at which secondary motion occurs owing to either mechanism.

It should be noted that a 51×51 mesh was used to obtain the solutions presented in figures 2 and 3, whereas the three-dimensional solutions use a coarser cross-sectional mesh, typically 15×15. The finer mesh was used primarily to ensure that the central roll in figure 3(*b*) was not a spurious truncation-error effect. In fact several pairs of two-dimensional solutions using both meshes were obtained. As already mentioned, the form of the motion was unchanged but, of course, numerical values of the solution variables were affected by the mesh change. For example, for $Ra = 1{\cdot}5 \times 10^5$ and $Pr = 0{\cdot}71$, the maximum stream-function value changed from 12·59 in the 15×15 solution to 10·78 in the 51×51 solution and the Nusselt number (see §4.5) changed from 5·44 to 5·10; for $Ra = 10^6$ and $Pr = 0{\cdot}71$ the changes were 27·34 to 17·14 and 8·60 to 9·12. The 15×15 mesh, although adequate at the lower Rayleigh number, is clearly only marginally satisfactory at the higher Rayleigh number. In the following discussion, the quantitative two-dimensional data used for comparison with the three-dimensional results were all obtained with the coarser mesh to eliminate mesh dependency from the comparison.

4.2. *Three-dimensional motion:* $Ra = 10^4$

There has been little speculation concerning the nature of three-dimensional effects occurring in a nominally two-dimensional roll as a result of the presence of the end walls normal to the axis of the roll. Aziz (1965) presented solutions for the case of a roll in a cube heated from below but did not discuss the structure of the flow. Chorin (1968) considered only the initial stages of the transient growth of a roll after the onset of instability in a layer of fluid heated from below and did not give quantitative details of the final steady state.

In fact, Davis (1967) has provided the only speculation in his discussion of the systems of two-dimensional rolls predicted by his analysis of a finite box heated from below under conditions close to critical for the onset of fluid motion. He observed that the interaction of a roll with an end wall is similar to the interaction of a rotating mass of fluid with a rigid flat plate normal to the axis of rotation of the fluid, a problem that was considered analytically by Bödewadt (1940). Bödewadt's analysis indicates that an axial flow is induced. However, Davis argued that this flow would be small since it arises from nonlinear terms in the governing equations and he was considering small amplitude convection for which the governing equations are linear. Moreover, for

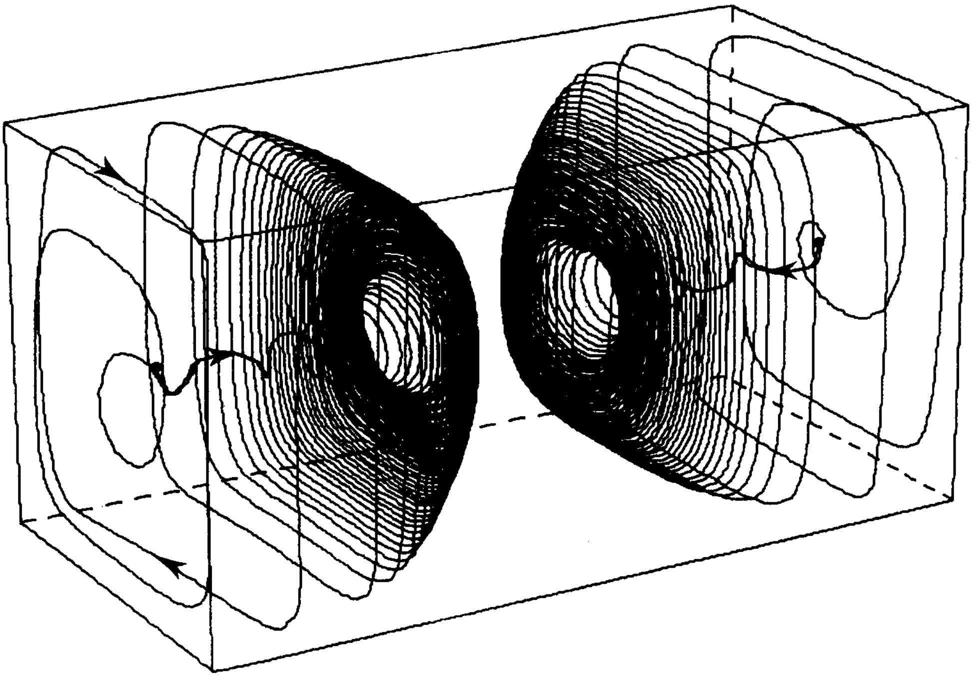

FIGURE 4. Streamlines through the points (0·45, 0·1, 0·45) and (0·45, 1·9, 0·45) in a window cavity with $Ra = 10^4$, $Pr = 1$, $h_y = 2$ and $h_z = 1$. The viewpoint used in the perspective transformation is $(-8, -4, -3)$.

small values of the local angular velocity, the boundary-layer thickness predicted by the Bödewadt theory is larger than the length of the roll; since the axial velocity must be zero at the end wall, Davis argued that for small rates of rotation the axial velocity throughout the roll must be very small. He concluded that, for small amplitude convection in a layer heated from below, three-dimensional effects are negligible. The validity of this conclusion will be challenged later. Davis was, however, correct in speculating that the presence of the end walls induces axial flow in a roll, thereby generating a three-dimensional motion.

In the window cavity, a single roll exists for $Ra \leqslant 6 \times 10^4$ and $0{\cdot}1 \leqslant Pr \leqslant 100$. The general form of the three-dimensional motion resulting from the superposition of the axial flow on the cross-sectional flow is displayed by the streamlines illustrated in figure 4. The box has been viewed from the same point as that used to obtain figure 1, so that the origin of the co-ordinate system is located on the nearest upper vertex of the box. This viewpoint was used to obtain all the perspective views of the $h_y = 2$ and $h_z = 1$ cavity.

The axial flow is directed away from each end wall, so that the streamlines spiral towards the centre of the box. In contrast to the infinite system postulated by Bödewadt, this axial flow must be countered by a return flow in x and z boundary layers. The streamlines spiral outwards near the $y = \frac{1}{2}h_y$ plane, return to the end walls in these layers and then spiral inwards near the end walls to form closed paths which lie on torus-like surfaces.

4.2.1. *On the closure of the streamlines.* The streamline illustrated in figure 4 returns to within a very small distance from the starting point of the track after only one circuit of the toroidal path and appears, therefore, to support the concept that the streamlines are closed. The conditions that $\nabla . \mathbf{v} = 0$ and the normal component of $\mathbf{v}$ at each boundary is zero lead to the conclusion that the streamlines must close, but as Truesdell (1954, p. 17) takes care to point out, a streamline through a given point may pass near that point many times before actual closure. Thus it is possible that the streamlines make many traverses of the type illustrated in figure 4 before closing.

The velocity field is single valued and streamlines cannot intersect. It follows that if a streamline makes several traverses then each traverse must lie on the same toroidal surface. If not, each successive traverse would lie on a smaller or larger surface which is contained by or contains the surface on which the previous traverse was made. In either case it is not possible for the line to return to the original surface without intersection of streamlines at some point in the cavity. Multiple traverses on the same surface without streamline intersection are, however, possible and cannot be rejected *a priori*.

The numerical tracking procedure is not capable of the accuracy required to investigate the question of closure of the streamlines. The closure indicated in figure 4 must be regarded as being accidental, bearing in mind that over 13 000 time steps were involved in computing the streamline. The majority of streamlines computed so far do not exhibit closure after only one such traverse.

4.2.2. *The inertial end effect.* The fluid adjacent to the end wall is stationary. This results in two mechanisms by which a three-dimensional flow can be produced. The first, which will be referred to here as inertial, is the kinematical interaction of the rotating fluid with the stationary plane as modelled by Bödewadt (1940). The second is thermal and results from axial temperature gradients (i.e. in the direction normal to the end walls) produced near the ends of the cavity by variations in the flow field. In this subsection we consider the first mechanism.

A more accurate model of the interaction of a rotating roll with an end wall than Bödewadt's infinite system is that of a rotating cylinder with a stationary end wall, for which numerical solutions were published by Pao (1970). At least for the case of a low Rayleigh number single roll, the approximation of the cross-sectional convection flow far from the end walls by a uniform rotation is tolerably good and Pao's solution may be used to estimate the magnitude of the end effect in either half of the cavity. In Pao's analysis, the flow depends upon a Reynolds number $Re = \Omega' R^2 \nu$, where R and Ω' are the radius and angular velocity of the cylinder respectively. From our results, we may first estimate Ω (a non-dimensional angular velocity) by taking averages along the lines $(x, \frac{1}{2}h_y, 0{\cdot}5)$ and $(0{\cdot}5, \frac{1}{2}h_y, z)$. Then, recalling that L and κL were used to construct our non-dimensional variables, we obtain $\Omega' = \Omega\kappa/L^2$. Hence we may compute a Reynolds number

$$Re = (\Omega\kappa/L^2)(R^2/\nu) = \Omega/4Pr,$$

where the 'radius' of our square cross-section has been taken as $\frac{1}{2}L$.

In table 1, Reynolds numbers for several values of Pr and $Ra = 10^4$ are given together with the maximum value in each case of the y velocity component on the axis of the roll, denoted by V_{axial}. It is immediately evident that Re is nearly inversely proportional to Pr. The magnitude of the axial flow can therefore also be expected to increase with decreasing Pr (for a given value of Ra) and this is supported by the values of V_{axial} and by the streamlines illustrated in figure 5.

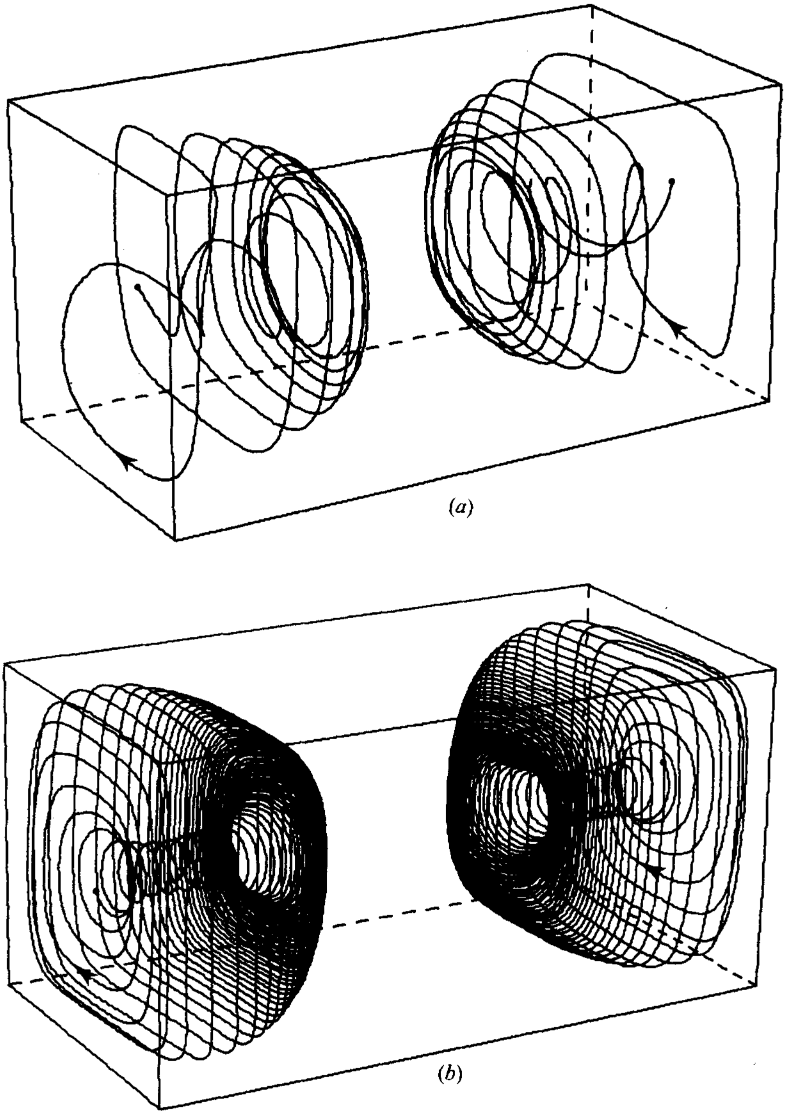

FIGURE 5. Streamlines through the points (0·4, 0·1, 0·4) and (0·4, 0·9, 0·4) with $Ra = 10^4$, $h_y = 2$ and $h_z = 1$. (a) $Pr = 0{\cdot}2$, (b) $Pr = 100$.

The only solution published by Pao (1970) for which the maximum value of the axial velocity component was quoted was for $Re = 100$ and a cylinder length-to-radius ratio of 1. To compare his result with the end effect in a window cavity, a further solution was obtained with $Ra = 10^4$, $Pr = 0{\cdot}1$, $h_y = 1$ and $h_z = 1$. Because of the nonlinear dependence of Ω on Pr and h_y it was difficult to obtain a solution for precisely the required value of Re. The estimated value of Ω for this solution is 37·6, leading to $Re = 94$. Pao predicted a maximum value of 0·1 for his non-dimensional axial velocity component. Noting that his scale factor for velocity was $\Omega' R$ ($= \Omega\kappa R/L^2$) whereas our scale factor is κ/L, this prediction corresponds to a non-dimensional velocity of $0{\cdot}1 R\Omega/L = 1{\cdot}88$ in our notation. V_{axial} in our convection solution is 2·47, which is

Pr	Ω	Re	V_{axial}
0·1	40	100	4·065
0·2	43	54	3·950
0·7	55	20	2·286
1·0	55	14	1·870
100·0	58	0·15	0·436

TABLE 1. Estimates of Ω and Re for several values of Pr for a cavity with $Ra = 10^4$, $h_y = 2$ and $h_z = 1$. V_{axial} is the maximum velocity along the axis of the roll.

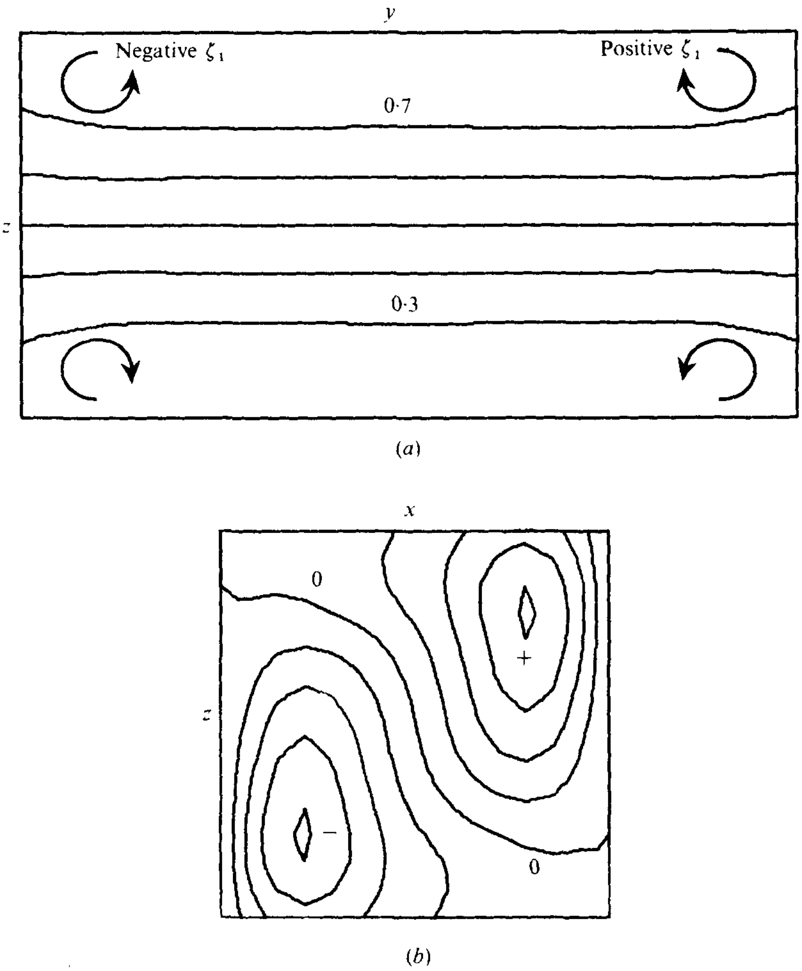

(*a*)

(*b*)

FIGURE 6. Longitudinal temperature variation in a window cavity with $Ra = 10^4$, $Pr = 100$, $h_y = 2$ and $h_z = 1$. (*a*) θ in the plane $x = 0{\cdot}5$; contour levels are 0·3 (0·1) 0·7. (*b*) $\partial\theta/\partial y$ in the plane $y = 0{\cdot}14$; contour levels are $-0{\cdot}4$ (0·1) 0·4.

significantly higher than Pao's prediction: higher than can be accounted for by the difference between the two values of *Re*. In addition, Pao's results indicate that for $Re \leqslant 10$ nonlinear effects are insignificant and the solution variables depend linearly on *Re*. This is not supported by the results in table 1, the last two lines of which show Reynolds numbers in the ratio of about 100 but axial velocities in the ratio of about 4. It is clear that the inertial model accounts for only part of the present end effect.

4.2.3. *The thermal end effect.* Near the $y = 0$ and $y = h_y$ boundaries, the fluid moves more slowly than it does far from the boundary, and the convection of heat is reduced. This reduction in convection near the end walls produces gradients of θ in the y direction. In figure 6 the distribution of θ near the end walls is indicated by two contour maps. That in figure 6(*a*) shows the temperature field on the plane $x = 0{\cdot}5$ and that in figure 6(*b*) the $\partial\theta/\partial y$ field in the plane $y = 0{\cdot}14$, in which the maximum value of $\partial\theta/\partial y$ occurs. Near the $y = 0$ boundary, the variation of $\partial\theta/\partial y$ is such that positive gradients (leading to negative ζ_1) predominate in the upper half of the cavity and negative gradients in the lower half. In figure 6(*a*) the reader is looking along the x axis; the predominant vorticity sign in each quarter of the cavity has been indicated. The generation of ζ_1 is such that the inertially induced axial flow is augmented by the thermal end effect.

If Pao's prediction of a linear dependence of the flow variables on *Re* for $Re \leqslant 10$ is accepted, a dependence which can only refer to the inertial end effect, then the flow field at $Pr = 100$, for which $Re \ll 1$, is essentially that arising from the thermal end effect. Moreover, the θ field changes insignificantly with *Pr* for $Pr \geqslant 0{\cdot}2$. For example, the maximum value of $\partial\theta/\partial y$ changes from 0·415 at $Pr = 100$ to 0·420 at $Pr = 0{\cdot}2$ and the contour maps for $Pr = 0{\cdot}2$ are virtually indistinguishable from those in figure 6. For $Pr < 0{\cdot}2$, the nonlinear effects of *Pr* on the convection become more significant and for $Pr = 0{\cdot}1$ the maximum gradient is reduced to 0·373. At least for $0{\cdot}2 \leqslant Pr \leqslant 100$ it is safe to assert that the thermal effect is independent of *Pr*.

The total longitudinal motion at any *Pr* is thus the sum of a constant thermal effect and a *Pr*-dependent inertial effect. The magnitude of the constant thermal effect can be deduced from a high Prandtl number solution, for which the inertial effect should be negligible. Thus table 1 shows that, for $Pr = 100$ and $h_y = 2$, the value of V_{axial} is 0·44. Noting (e.g. from figure 6*a*) that the thickness of the thermal boundary layer at each end of the cavity is about 0·25, this value may also be taken as applying to a cavity with $h_y = 1$ and moreover must be an estimate of the thermal effect at *any Pr*. When we add Pao's estimate of 1·88 for the inertial end effect at $Pr = 0{\cdot}1$ (see §4.2.2 above), we obtain a total axial velocity of 2·32, in quite good agreement with the value of 2·47 found in our convection solution.

4.2.4. *Vortex lines.* In a two-dimensional flow, the vortex lines are normal to the plane of the flow and are infinite in length. In the core of a roll where the vorticity is positive, the lines are in the $+y$ direction; in the viscous boundary layers they are in the opposite direction.

In the three-dimensional case, the no-slip boundary condition deflects the vortex lines at the end walls, so that they form closed loops. The vorticity field is solenoidal and subject to the same general comments regarding closure as is the velocity field. However, the symmetry of the field about the $y = \frac{1}{2}h_y$ plane guarantees that the vortex lines form single closed loops.

Typical vortex lines for two of the $Ra = 10^4$ solutions are illustrated in figure 7. In

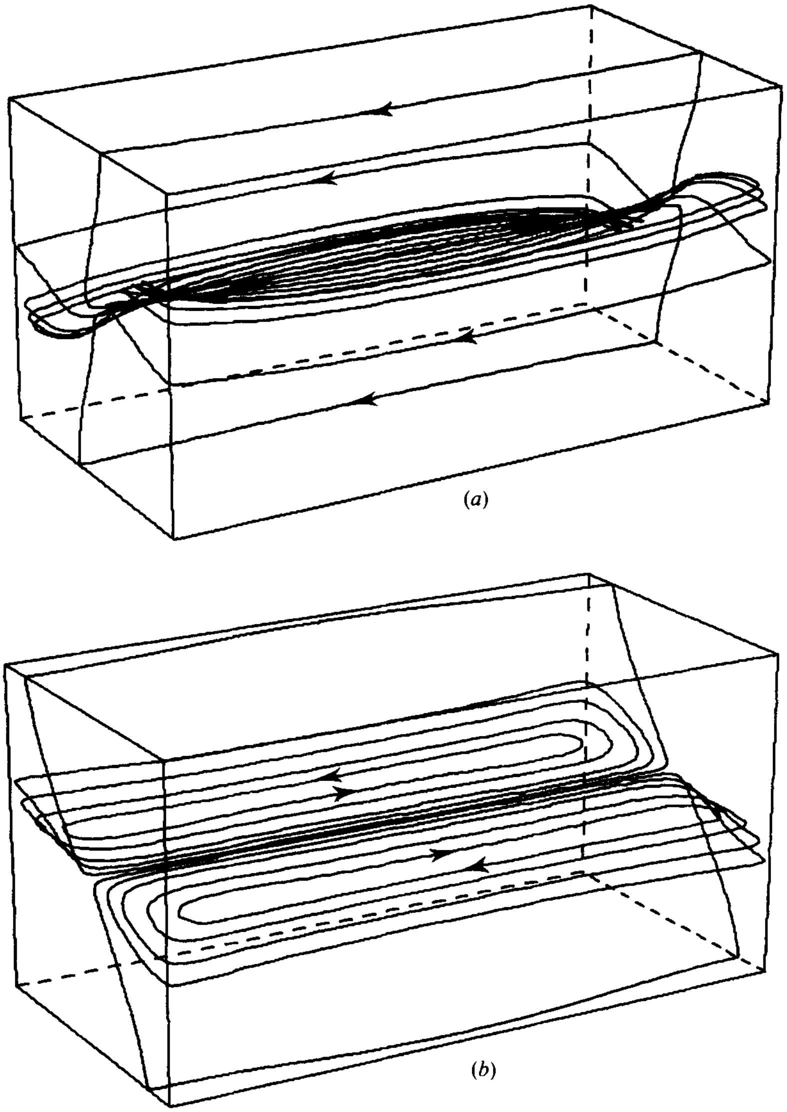

FIGURE 7. Vortex lines passing through points on the line $(x, 1{\cdot}0, 0{\cdot}5)$ in window cavities with $Ra = 10^4$, $h_y = 2$ and $h_z = 1$. (a) $Pr = 0{\cdot}2$, (b) $Pr = 100$.

each diagram the vortex lines pass through points on the line $(x, 1, \frac{1}{2})$. The solution in figure 7(a) is for $Pr = 0{\cdot}2$ and the vortex lines are noticeably twisted near each end wall, having been convected by the rotating flow as they are deflected to conform with the requirements of the no-slip boundary condition. Twisting of vortex lines in this manner produces a velocity component along the axis of twist. In contrast, the lines in figure 7(b) for $Pr = 100$ are not twisted, reflecting the fact that the convection of vorticity is negligible at the higher value of Pr. The vortex lines in this way clearly illustrate the mechanism of the inertial effect as being that of the convection of vorticity by the velocity field (thereby justifying the term inertial) and confirm the conclusion that at $Pr = 100$ the inertial effect is negligible.

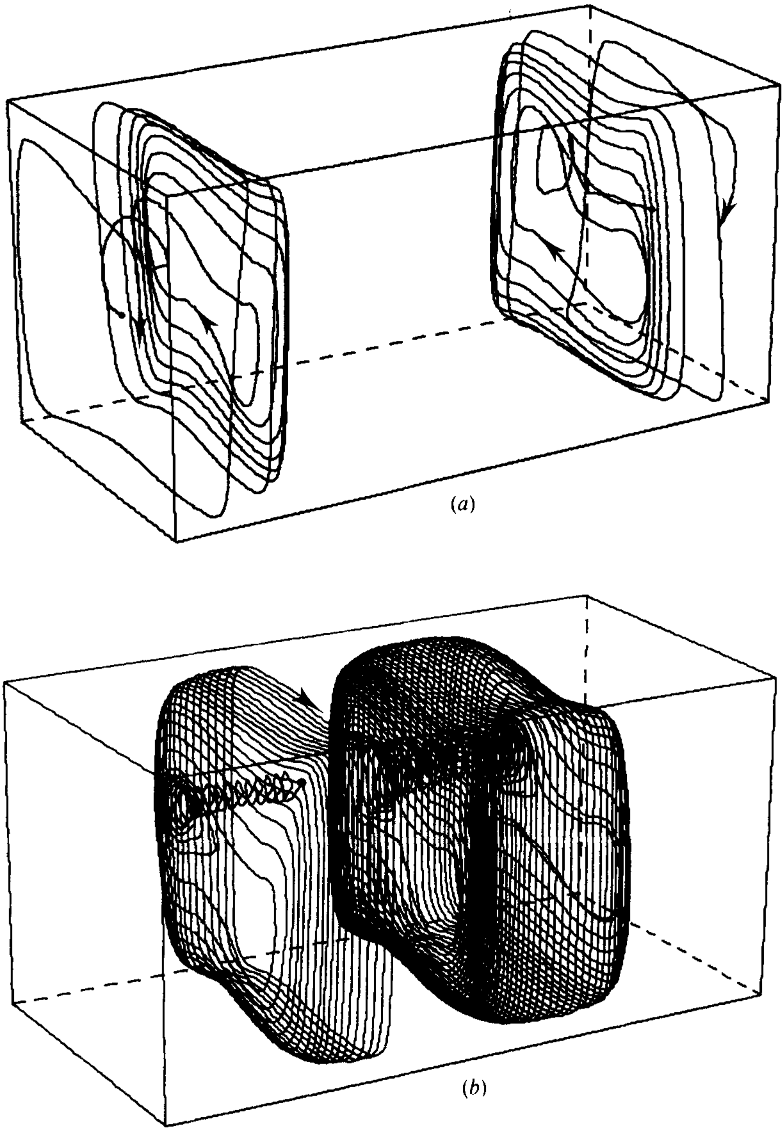

FIGURE 8. Flow in a window cavity with $Ra = 1{\cdot}5\times10^5$, $Pr = 0{\cdot}71$, $h_y = 2$ and $h_z = 1$. (*a*) Streamlines through the points (0·5, 0·1, 0·51) and (0·5, 1·9, 0·51), showing the forward flow. (*b*) Streamlines through the points (0·7, 0·8, 0·35) and (0·7, 1·2, 0·35), showing the reverse flow.

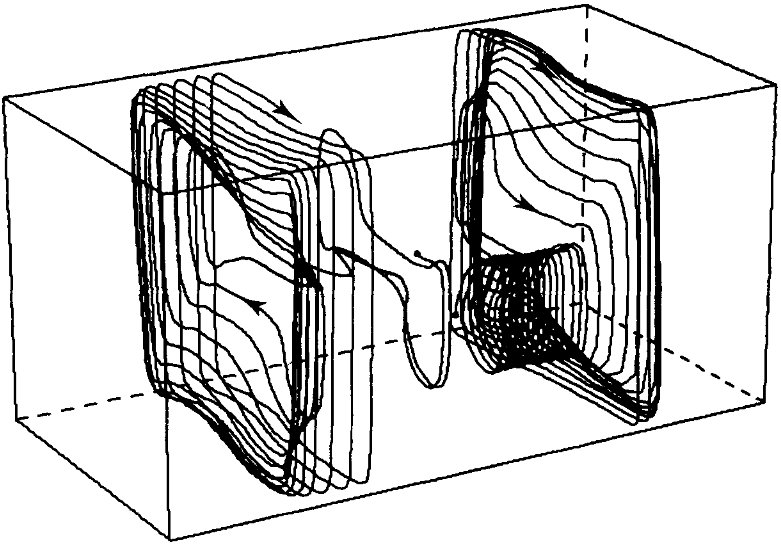

FIGURE 9. Reverse flow in a window cavity with $Ra = 5\times10^5$, $Pr = 0{\cdot}71$, $h_y = 2$ and $h_z = 1$.

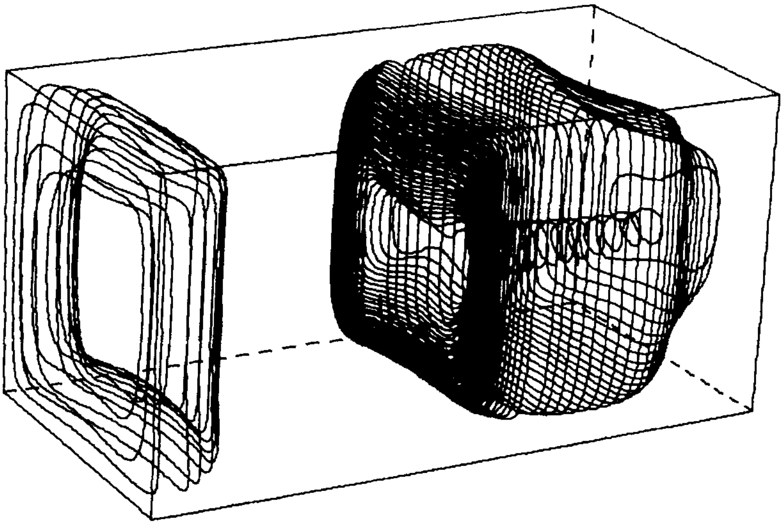

FIGURE 10. Flow in a cavity with $Ra = 1{\cdot}5\times10^5$, $Pr = 100$, $h_y = 2$ and $h_z = 1$. The streamline in the left half of the cavity belongs to the forward flow adjacent to the end wall. The streamline in the right half belongs to the reverse flow.

4.3. *Three-dimensional motion*: $Ra \geqslant 6\times10^4$

As the Rayleigh number is increased, the structure of the three-dimensional flow is complicated by the occurrence of secondary motion. For $Ra = 1{\cdot}5\times10^5$, $Pr = 0{\cdot}71$, $h_y = 2$ and $h_z = 1$, the cross-sectional flow far from the end walls (i.e. viewed along the y axis) contains two secondary rolls similar to those shown in figure 2 (*d*). Some aspects of the three-dimensional flow are illustrated in figure 8. The streamlines in figure 8 (*a*) indicate that a strong axial flow exists near each end wall. The main difference between

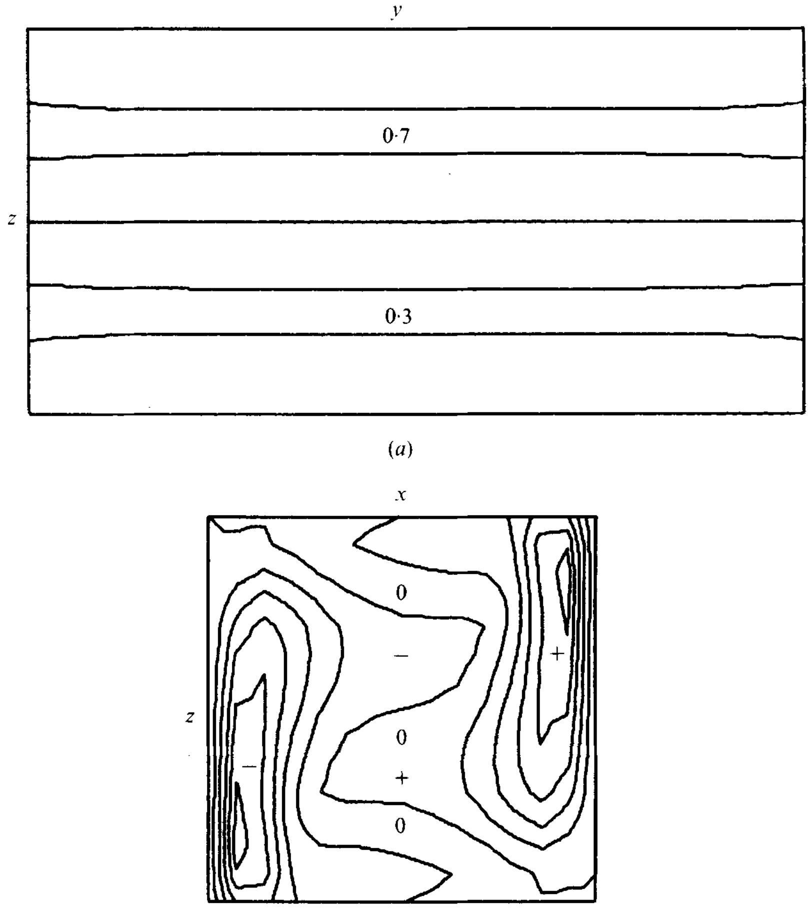

(*a*)

(*b*)

FIGURE 11. Longitudinal temperature variation in a window cavity with $Ra = 1{\cdot}5 \times 10^5$, $Pr = 100$, $h_y = 2$ and $h_z = 1$. (*a*) θ in the plane $x = 0{\cdot}5$; contour levels are 0·3 (0·1) 0·7. (*b*) $\partial\theta/\partial y$ in the plane $y = 0{\cdot}14$; contour levels are $-0{\cdot}5$ (0·1) 0·5.

this flow and that in the single-roll flow at $Ra = 10^4$ is that *each* of the secondary rolls forms a spiral centre for the inward moving fluid.

The end effect is, however, confined to the vicinity of the end wall and is separated from the centre-plane by a reverse flow which is illustrated by the streamlines in figure 8(*b*). (Note the convention introduced here: that a *forward* flow has the inner axial flow moving *away* from the nearer end wall.) This streamline was started from a point which is almost on the axis of the secondary roll adjacent to the hot wall, and near the mid-plane $y = \frac{1}{2}h_y$ of the box. It spirals *back* towards the end wall, meets the opposing forward flow and spirals out to the boundary layers, where it returns towards the mid-plane. The streamline in the left half of the cavity was terminated at this stage, but the continuation to form a nearly closed path is shown as a mirror image in the right half of the cavity.

For $Pr = 0{\cdot}71$, this flow structure exists for $6 \times 10^4 \leqslant Ra \leqslant 3 \times 10^5$. For $Ra > 3 \times 10^5$, the cross-sectional flow develops a central secondary roll as in the two-dimensional solution of figure 3(*b*). In this flow all three secondary rolls act as spiral centres for the

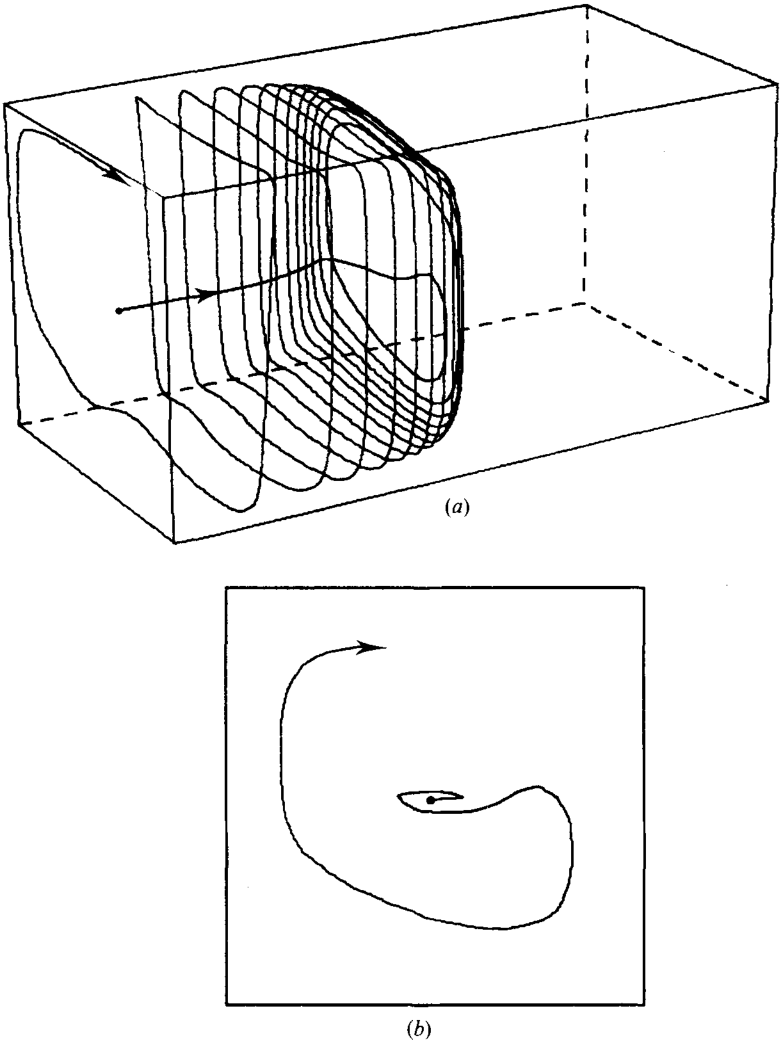

FIGURE 12. (a) Streamline through the point (0·49, 0·1, 0·49) in a cavity with $Ra = 1{\cdot}5 \times 10^5$, $Pr = 0{\cdot}2$, $h_y = 2$ and $h_z = 1$. (b) The first part of the streamline in (a) viewed by looking parallel to the y axis.

reverse flow. The streamlines in figure 9 for $Ra = 5 \times 10^5$ and $Pr = 0{\cdot}71$ both belong to the reverse flow. The streamline in the left half of the cavity has used the central roll as a spiral centre whilst that in the right half has used the roll adjacent to the cold wall.

Detailed examination of the solution has indicated that the velocity along the axis of each outer roll is directed *towards* the $y = \frac{1}{2}h_y$ plane along the entire length of the roll and is zero at the boundary between the forward and reverse flows. Streamline tracks reveal that a self-contained *forward* flow exists within the envelope defined approximately by the first part of the streamline in the right half of figure 9, the vertical plane through the point where that streamline begins to spiral outwards, and the $y = \frac{1}{2}h_y$ plane (i.e. within the *reverse* flow illustrated). This flow is very weak; it was impossible

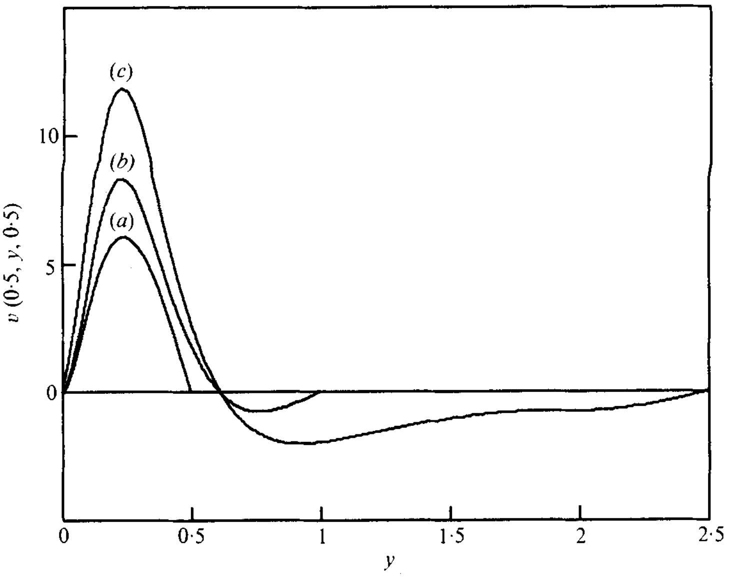

FIGURE 13. Variation of v along the horizontal axis of a cavity with $Ra = 5 \times 10^5$, $Pr = 0{\cdot}71$ and $h_z = 1$. (*a*) $h_y = 1$. (*b*) $h_y = 2$. (*c*) $h_y = 5$.

to obtain streamlines that indicated the form of the flow and were capable of satisfactory reproduction.

As in the case of the $Ra = 10^4$ flow, a change in Pr at constant Ra has a considerable effect on the three-dimensional flow. Several solutions for $Ra = 1{\cdot}5 \times 10^5$ and various values of Pr were obtained. For $Pr \geqslant 10$, the axial flow is independent of Pr and the three-dimensional motion has the structure indicated by the streamlines in figure 10. The motion in each half of the cavity consists of two distinct flows as in the $Pr = 0{\cdot}71$ solution. However, the reverse flow nearly fills the half-cavity and the fluid spirals from the $y = \frac{1}{2}h_y$ plane to the end walls using either secondary roll as a spiral centre. The forward flow is confined to a small torus-shaped region at the end of the cavity. In the interests of clarity, only one streamline has been drawn in each half of the cavity. In the left half a forward torus-shaped streamline has been constructed. In the right half, the form of the reverse flow is shown. The space taken by the forward flow in that half of the cavity, and the manner in which the two flows jointly occupy each half-cavity, can be seen. The reverse flow penetrates into the region of forward flow, so that the surface separating the two regions is not plane but convex to the ends of the cavity.

The invariance of the flow with Pr for $Pr \geqslant 10$ suggests that the flow illustrated in figure 10 is purely the result of longitudinal buoyancy effects. Isotherms for the plane $x = \frac{1}{2}$ are shown in figure 11 (*a*) and indicate that, near the ends of the cavity, the sign of $\partial\theta/\partial y$ near the axis of rotation is opposite to that near the z boundaries. This is confirmed by the contours of $\partial\theta/\partial y$ in the plane $y = 0{\cdot}14$ illustrated in figure 11 (*b*). The forward spiral results from the strong gradients in the lower left and upper right corners of the cross-section, where the effects of reduced convection near the end walls are greatest (cf. figure 2*a*). The reverse flow is the result of gradients induced in the centre of the cross-section, where the convective effects of the secondary rolls are greatest.

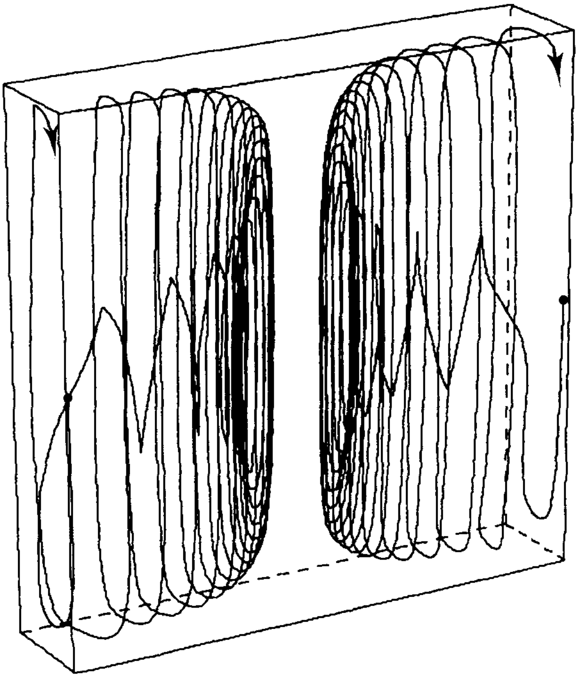

FIGURE 14. Streamlines through the points (0·04, 0·04, 2·5) and (0·04, 4·96, 2·5) in a window cavity with $Ra = 10^4$, $Pr = 0{\cdot}71$, $h_y = 5$ and $h_z = 5$. Viewpoint is $(-30, -15, -10)$.

The flow in figure 8 for $Pr = 0{\cdot}71$ represents a state intermediate between the infinite Pr flow and that at very small Pr, when the inertial end effect is so strong that the forward spiral completely fills each half of the cavity. The latter case is illustrated by the streamline in figure 12. The cross-sectional flow in the $y = \frac{1}{2}h_y$ plane is a system of three rolls similar to that in figure 2 (*f*); each secondary roll acts as a spiral centre. The interesting feature of the streamline illustrated in figure 12 (*b*) is that, because it uses the counter-rotating central roll as a spiral centre, it initially spirals anticlockwise (in the sense of figure 12*b*) before reaching the clockwise main flow.

4.4. *The dependence of the three-dimensional flow on h_y and h_z*

So far, the discussion has been almost entirely devoted to a cavity with $h_y = 2$ and $h_z = 1$. Although a detailed discussion of the influence of either aspect ratio on the flow would require many more solutions than have been obtained, the following observations have been made from two groups of solutions at other aspect ratios. The solutions in the first group have $h_z = 1$ and $1 \leqslant h_y \leqslant 5$ so that the effect of the longitudinal aspect ratio on the flow in a cavity of square cross-section may be examined. In the second group, $h_y = 5$ and $h_z = 5$ so that the solutions represent more closely the flow in a real double-glazed window.

In general, both the strength of the rotational flow and the form and strength of the end effect depend on the longitudinal aspect ratio. The driving buoyancy forces established by the temperature difference between the isothermal walls must overcome the viscous drag at each end wall. The strength of the cross-sectional flow as measured,

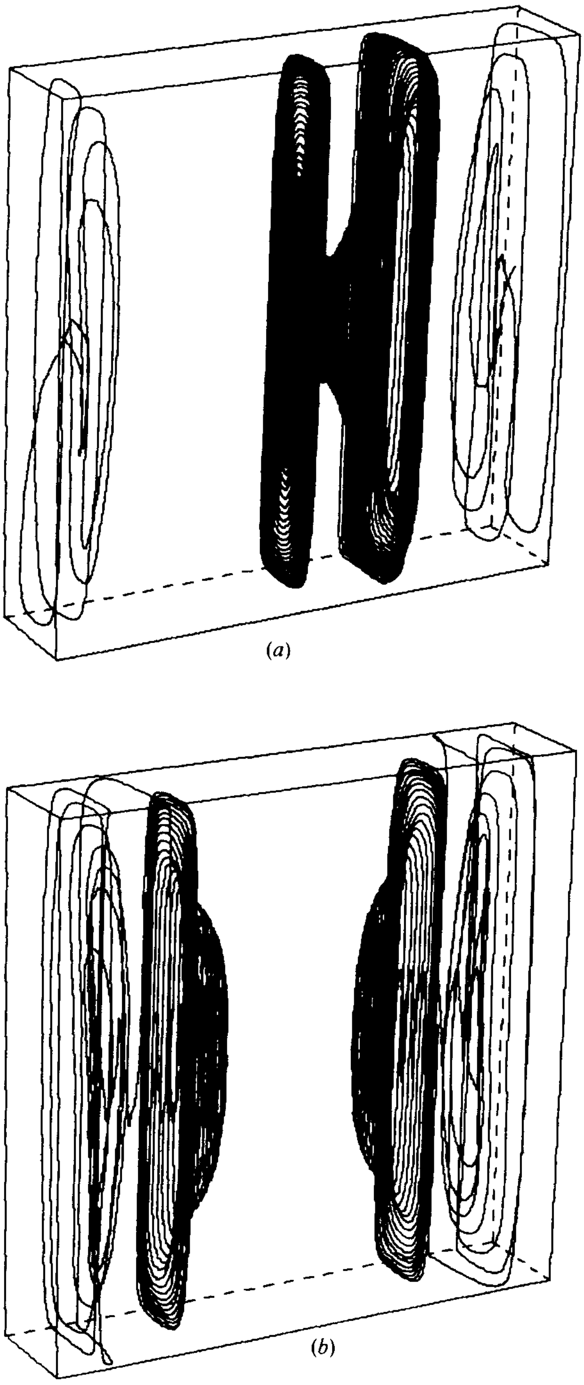

FIGURE 15. Flow in a window cavity with $Ra = 3\times 10^4$, $Pr = 1$, $h_y = 5$ and $h_z = 5$. (*a*) The streamlines at each end of the cavity indicate a strong forward flow. In the right half of the cavity a streamline indicating a weak forward flow adjacent to the centre-plane has been included. (*b*) These streamlines indicate the reverse flow of intermediate strength that exists between the two forward flows shown in (*a*).

Ra	Pr	h_y	$\psi_2^{\max}$	$\psi_{2D}^{\max}$
$1{\cdot}5\times10^5$	1	1	13·0	13·3
$1{\cdot}5\times10^5$	1	2	13·2	13·3
$1{\cdot}5\times10^5$	1	5	13·3	13·3
5×10^5	0·71	1	18·4	19·8
5×10^5	0·71	2	19·7	19·8
5×10^5	0·71	5	19·8	19·8

TABLE 2. Comparison of the maxima of ψ_2 in the plane $y = \frac{1}{2}h_y$ with the two-dimensional stream-function maxima.

for example, by the maximum value of ψ_2 in the $y = \frac{1}{2}h_y$ plane, denoted by $\psi_2^{\max}$, will depend on the magnitude of the drag relative to the total buoyancy torque applied along the length of the cavity. $\psi_2^{\max}$ can be expected to decrease with decreasing h_y.

In table 2, values of $\psi_2^{\max}$ are listed for $h_y = 1$, 2 and 5 and for two combinations of Ra and Pr, namely $Ra = 1{\cdot}5\times10^5$ and $Pr = 1$, and $Ra = 5\times10^5$ and $Pr = 0{\cdot}71$. For comparison, the corresponding value of the stream-function maximum as predicted by a two-dimensional solution with the same cross-sectional mesh is also given. In every case the strength of the flow in the $y = \frac{1}{2}h_y$ plane in the three-dimensional solutions is less than or equal to that in the two-dimensional flow. The strength of the flow is not significantly affected for $h_y \geqslant 2$. But for $h_y = 1$ the reduction in the case of the solution for $Ra = 1{\cdot}5\times10^5$ is 2·3 % of the two-dimensional strength, increasing to 7 % in the case of the stronger flow at $Ra = 5\times10^5$.

The form of the three-dimensional flow in a cavity with $h_y \geqslant 2$ for both combinations of Ra and Pr is that of a system of forward and reverse flows as illustrated in figure 8. The solutions for $h_y = 2$ and $h_y = 5$ suggest that, once the reverse flow is established, the penetration of the forward flow into the cavity is independent of h_y. This is demonstrated in figure 13 by the distributions of v on the line (0·5, y, 0·5) in the semi-cavity $0 \leqslant y \leqslant \frac{1}{2}h_y$ for the three values of h_y and for $Ra = 5\times10^5$ and $Pr = 0{\cdot}71$. For $h_y = 2$ and $h_y = 5$, the penetration of the forward spiral is approximately 0·6. In a cavity with $h_y = 1$, the reverse flow does not occur.

In the case of infinite Pr, the forward-flow penetration distance is determined primarily by the thickness of the thermal boundary layer, which, as indicated by the results in the next subsection, is less than 0·4. The flow can be expected to be substantially the same as that illustrated in figure 10. The torus-shaped forward flow remains fixed in size irrespective of the value of h_y.

An increase in h_z reveals an interesting phenomenon. At $Ra = 10^4$ and $Pr = 0{\cdot}71$ in a cavity with $h_y = 5$ and $h_z = 5$, the flow resembles that in the $h_z = 1$ cavity in that the end effect is a single axial flow embedded in the single-roll cross-sectional flow. A single spiral system, illustrated in figure 14, is produced. However, for $Ra > 10^4$ the axial flow decomposes into a series of forward and reverse spirals, despite the fact that the cross-sectional flow is known to be a single roll (see Rubel & Landis 1969). For example, at $Ra = 3\times10^4$ and $Pr = 1$ there are three distinct flows in each half of the cavity. The forward flows at the ends of the cavity are by far the strongest, and correspond to large peaks in the distribution of $v(0{\cdot}5, y, 2{\cdot}5)$. Typical streamlines are illustrated in figure 15. Reverse flows (figure 15b) separate the end flows from a further pair of forward flows adjacent to the plane $y = \frac{1}{2}h_y$. One streamline for the right-hand inner

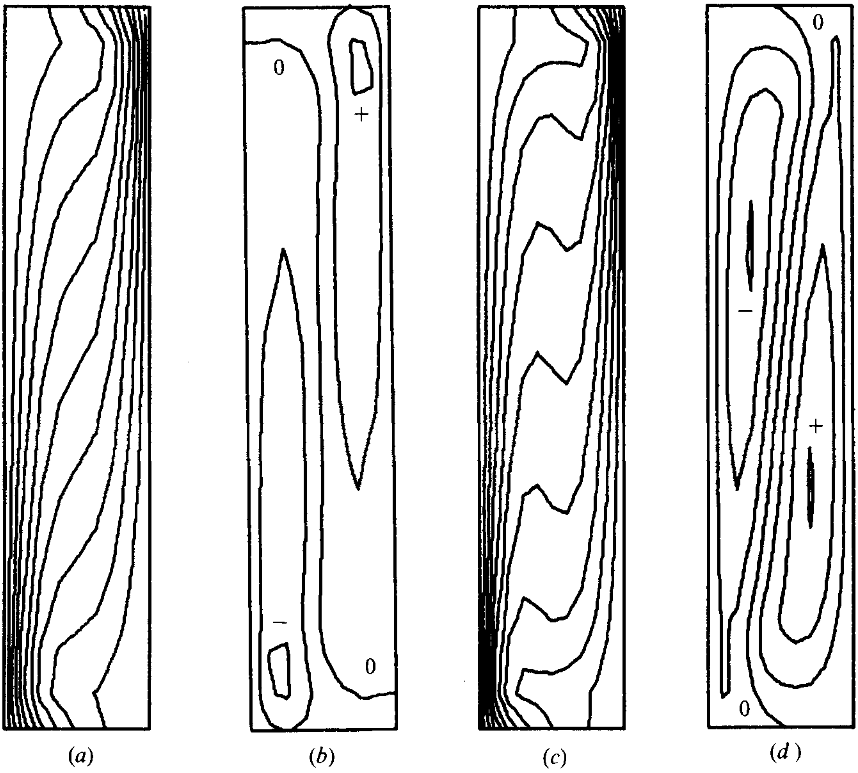

FIGURE 16. Temperature field in a cavity with $h_y = h_z = 5$. (*a*, *b*) $Ra = 10^4$ and $Pr = 0{\cdot}71$. (*c*, *d*) $Ra = 3 \times 10^4$ and $Pr = 1$. (*a*, *c*) θ in the plane $y = 2{\cdot}5$; contour levels are 0·1 (0·1) 0·9. (*b*, *d*) $\partial\theta/\partial y$ in the plane $y = 0{\cdot}37$; contour levels in (*b*) are −0·2 (0·1) 0·2; contour levels in (*d*) are −0·15 (0·05) 0·15.

forward flow is shown in figure 15. The closeness of the spacing between adjacent turns of the spiral emphasizes the weakness of the axial motion in this innermost forward flow.

The occurrence of the multiple longitudinal flows appears to be associated with the development of a region of negative $\partial\theta/\partial x$ in the centre of the cavity cross-section as shown by the isotherms in the plane $y = 2{\cdot}5$ for the $Ra = 3 \times 10^4$ solution (figure 16*c*). These isotherms are to be compared with the corresponding isotherms for the $Ra = 10^4$ solution, shown in figure 16(*a*). At the lower value of Ra the contours of $\partial\theta/\partial y$ in the plane $y = 0{\cdot}37$ indicate that $\partial\theta/\partial y$ is predominantly positive in the upper half of the cross-section whereas the contours for the same plane in the $Ra = 3 \times 10^4$ solution indicate that the sign of $\partial\theta/\partial y$ is such that the ζ_1 generated will oppose the inertial effect. This explains the confinement of the forward flow near the end wall in the case of the greater value of Ra.

The multiplicity of the longitudinal flow is associated with spatial oscillations of the temperature field in the y direction which may be the result of a physical instability of the flow with respect to disturbances that are periodic in y as is the case in the inclined layer studied by Hart (1971). Certainly, attempts here to obtain solutions for

$$Ra \geqslant 3 \times 10^4$$

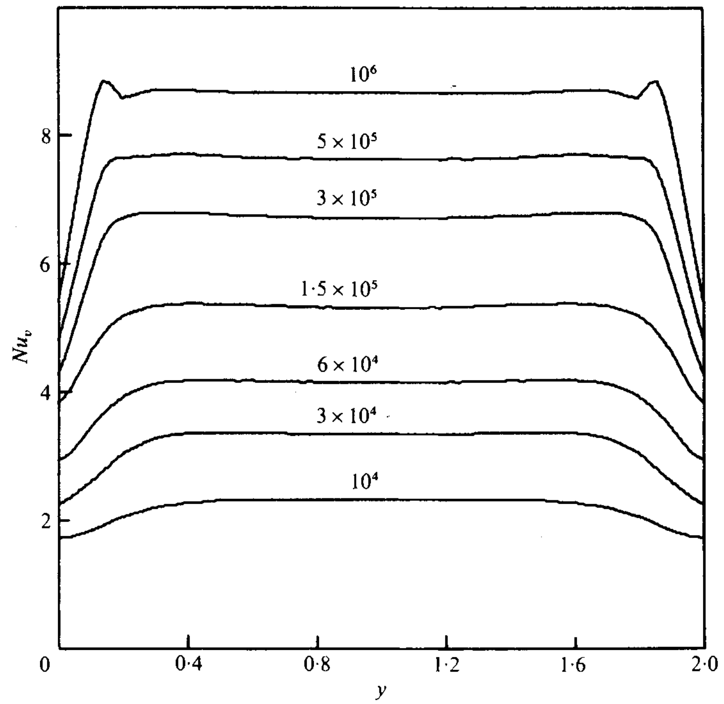

FIGURE 17. The functions $Nu_v(y)$ for a cavity with $Pr = 0{\cdot}71$, $h_y = 2$ and $h_z = 1$ for several values of Ra.

failed not from numerical instability but from an inability to reach a steady solution: this suggests a physical instability with respect to travelling disturbances.

4.5. *The effect of the three-dimensional motion on heat transfer*

The non-dimensional local heat flux through a boundary may be represented by a Nusselt number

$$Nu = \partial\theta/\partial n, \tag{12}$$

where n is the co-ordinate normal to the boundary. On the isothermal wall at $x = 0$

$$Nu(y,z) = [\partial\theta/\partial x]_{x=0}.$$

In laboratory experiments, the estimation of the total heat transfer through the cavity is often the prime objective and may in fact be the only parameter measured. For the wall at $x = 0$, the total flux is given by

$$h_y h_z Nu_{\text{av}} = \int_0^{h_z}\int_0^{h_y} Nu(y,z)\,dy\,dz,$$

where Nu_{av} is the average Nusselt number for the wall. In a two-dimensional model, the local heat flux is a function only of z and the average flux, denoted here by Nu_{2D}, is given by

$$h_z Nu_{\text{2D}} = \int_0^{h_z} Nu(z)\,dz.$$

Ra	Nu_{2D}	Nu_{av}	Nu_{vm}	$\dfrac{Nu_{av}-Nu_{2D}}{0{\cdot}01Nu_{2D}}$	$\dfrac{Nu_{vm}-Nu_{2D}}{0{\cdot}01Nu_{2D}}$
10^4	2·31	2·20	2·32	−4·8	0·4
3×10^4	3·32	3·18	3·33	−4·2	0·3
6×10^4	4·11	4·00	4·14	−2·7	0·7
$1{\cdot}5\times10^5$	5·28	5·14	5·30	−2·7	0·4
3×10^5	6·67	6·53	6·69	−2·1	0·3
5×10^5	7·58	7·43	7·62	−2·0	0·5
1×10^6	8·59	8·37	8·67	−2·6	0·9

TABLE 3. Comparison of Nu_{av} and Nu_{vm} with Nu_{2D} for a cavity with $h_y = 2$, $h_z = 1$, $Pr = 0{\cdot}71$ and $10^4 \leqslant Ra \leqslant 10^6$.

In the three-dimensional model it is informative to compute the vertical average of the Nusselt number Nu_v at any value of y:

$$h_z Nu_v(y) = \int_0^{h_z} Nu(y,z)\,dz.$$

Numerically, the local heat flux was estimated by a three-point forward-difference approximation to the derivative in (12). The composite trapezoidal rule was then used to compute the averages.

The function $Nu_v(y)$ is shown in figure 17 for a cavity with $h_y = 2$ and $h_z = 1$ for $Pr = 0{\cdot}71$ and several values of Ra. Corresponding values of Nu_{av}, Nu_{vm} (the value of $Nu_v(y)$ at $y = \frac{1}{2}h_y$) and the two-dimensional estimate Nu_{2D} are listed in table 3. $Nu_v(y)$ decreases as each end wall is approached and indicates the extent of the thermal boundary layer, in which convection of heat is reduced. As Ra increases, the thickness of this layer decreases.

As shown in figure 17, $Nu_v(y)$ increases as $y \rightarrow 0$ or $y \rightarrow 2$ until the end boundary layer is reached. The gradual increase results from the increasing magnitude of the longitudinal velocity component in the boundary layer as the end wall is approached. The oscillation in $Nu_v(y)$ for $Ra = 10^6$ is probably caused by truncation errors associated with the finite-difference approximations and indicates that a finer mesh is required to model the flow accurately for $Ra \geqslant 10^6$.

The average Nusselt number is, in every case, lower than that predicted by the two-dimensional model. With the exception of the $Ra = 10^6$ result, the percentage changes listed in table 3 show that the end effect has a decreasing influence on Nu_{av} as the Rayleigh number increases; this can be attributed to the reduction in the thickness of the end-wall boundary layer with increasing Ra. An interesting observation is that Nu_{vm} is always greater than Nu_{2D}, albeit in many cases by a very small amount. This contrasts with the fact that $\psi_2^{\max}$, and hence the volume flux in this plane, is always *less* than the two-dimensional $\psi^2_{\max}$. This shows that, outside the thermal boundary layer at the ends of the cavity, the contribution of the axial flow to the convection of heat is more than sufficient to offset the influence of the reduction of the cross-sectional flow by the drag induced by the end walls.

Predictably, the relative difference between Nu_{av} and Nu_{2D} is inversely dependent on h_y as the results in table 4 confirm. This trend is superimposed on the Rayleigh number dependence, so that the greatest differences occur for small Ra and h_y. An

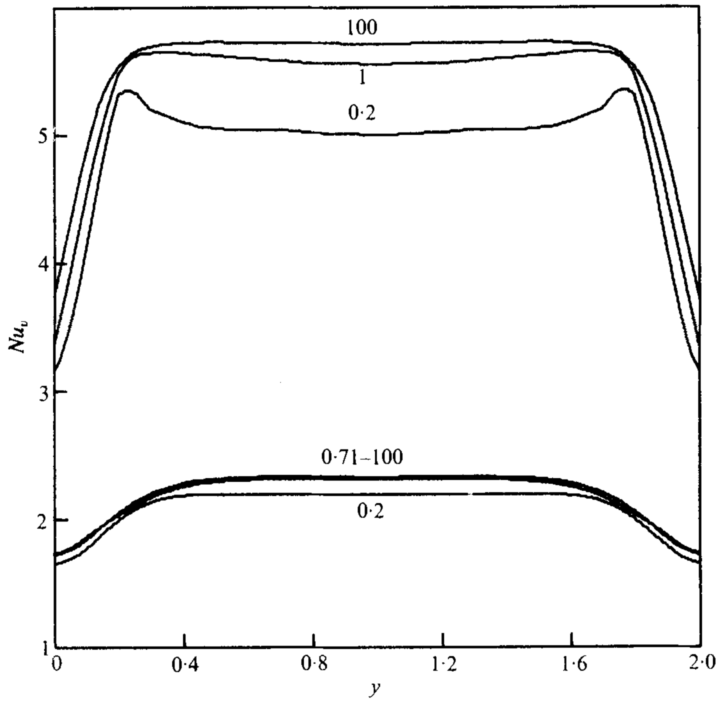

FIGURE 18. The function $Nu_v(y)$ in a cavity with $h_y = 2$ and $h_z = 1$. The lower group of curves is for $Ra = 10^4$ and the upper group is for $Ra = 1{\cdot}5 \times 10^5$. Values of Pr are marked on the figure.

interesting observation is that Nu_{2D} is a better estimate of Nu_{vm} than it is of Nu_{av}; but it is the latter that is measured in a physical experiment.

If Pr is varied whilst all other parameters are held constant, the axial flow increases with decreasing Pr. For the single-roll flow at $Ra = 10^4$ the effect on Nu_v is negligible for $0{\cdot}71 \leqslant Pr \leqslant 100$ (figure 18) and a slight reduction in heat transfer is evident for $Pr = 0{\cdot}2$; this is largely the result of changes in the cross-sectional flow. At

$$Ra = 1{\cdot}5 \times 10^5$$

the changes in the axial flow with Pr have a much greater effect on Nu_v for

$$0{\cdot}2 \leqslant Pr \leqslant 1.$$

When $Pr = 0{\cdot}2$, the forward end effect fills the semi-cavity. The large peak in Nu_v corresponds to large v in the boundary layers near the end of the cavity. The peaks are small in the curve for $Pr = 1$, when the flow consists of forward and reverse flow, and are absent when the thermally driven reverse flow nearly fills the cavity at $Pr = 100$. The corresponding Nusselt numbers are listed in table 5. For low Pr, Nu_{vm} is less than Nu_{2D}, in contrast to the situation at higher values of Pr. For $Pr \leqslant 0{\cdot}2$, the end effect decreases the strength of the cross-sectional flow considerably; the resultant reduction in heat transfer more than counteracts the increase due to the axial velocity component.

The two solutions at $h_y = h_z = 5$ indicate that Nu_v is essentially constant over 80 % of the length of the cavity and displays peaks at each end of the cavity, where the axial

Case	h_y	Nu_{2D}	Nu_{av}	Nu_{vm}	$\dfrac{Nu_{av}-Nu_{2D}}{0{\cdot}01Nu_{2D}}$	$\dfrac{Nu_{vm}-Nu_{2D}}{0{\cdot}01Nu_{2D}}$
A	1	5·54	5·31	5·71	−4·2	3·1
A	2	5·54	5·37	5·55	−3·1	0·2
A	5	5·54	5·41	5·54	−2·3	0·0
B	1	7·58	7·37	7·77	−2·8	2·5
B	2	7·58	7·43	7·62	−2·0	0·5
B	5	7·58	7·52	7·59	−0·8	0·1

TABLE 4. Comparison of Nu_{av} and Nu_{vm} with Nu_{2D} for cavities with $1 \leqslant h_y \leqslant 5$ and $h_z = 1$ for two combinations of *Ra* and *Pr*. In case *A*, $Ra = 1{\cdot}5\times10^5$ and $Pr = 1$. In case *B*, $Ra = 5\times10^5$ and $Pr = 0{\cdot}71$.

Ra	*Pr*	Nu_{2D}	Nu_{av}	Nu_{vm}	$\dfrac{Nu_{av}-Nu_{2D}}{0{\cdot}01Nu_{2D}}$	$\dfrac{Nu_{vm}-Nu_{2D}}{0{\cdot}01Nu_{2D}}$
10^4	0·2	2·21	2·08	2·19	−5·9	−0·9
10^4	1·0	2·32	2·20	2·32	−5·1	0·0
10^4	100	2·30	2·18	2·31	−5·2	0·4
$1{\cdot}5\times10^5$	0·2	5·11	4·89	5·00	−4·3	−2·2
$1{\cdot}5\times10^5$	1	5·54	5·37	5·55	−3·1	0·2
$1{\cdot}5\times10^5$	100	5·69	5·52	5·72	−3·0	0·5

TABLE 5. Effect of *Pr* on the comparison of Nu_{av} and Nu_{vm} with Nu_{2D} for a cavity with $h_y = 2$ and $h_z = 1$.

flow is large. The three-dimensional average Nusselt number is within 2·5 % of the two-dimensional estimate in both cases and Nu_{vm} and Nu_{2D} agree to within three significant figures.

5. Conclusions

The solutions to the problem of natural convection in a box presented here have revealed the existence of a three-dimensional end effect, the form of which depends delicately on the governing parameters. The effect arises from two mechanisms. An inertial mechanism dominates when *Pr* is small, whereas, when *Pr* is large, this mechanism diminishes and a weaker thermal effect dominates.

In terms of the average Nusselt number, which is often the end result of an experimental programme, the longitudinal motion has greatest relative effect for low *Ra*, small h_y and low *Pr*. It has least effect for a given value of *Ra* when h_y and *Pr* are large. In all cases, the two-dimensional estimate of the Nusselt number is a better estimate of the vertical average at the centre of a three-dimensional cavity than it is of the overall average.

In the single-roll flow for $Ra \sim 10^4$, the end effect in each half of the cavity produces an axial flow which is always directed towards the centre of the cavity. At the onset of secondary motion in a cavity with $h_z = 1$ and the development of negative $\partial\theta/\partial x$ in a cavity with $h_z = 5$, the longitudinal motion decomposes into multiple flows. For the case of a cavity filled with air, the numerical solutions predict that the end effect is confined to the vicinity of the end walls for $Ra \geqslant 6\times10^4$, and is separated from the centre of the cavity by a weak reverse flow which can be regarded as being essentially two-dimensional. For $6 \times 10^4 \leqslant Ra \leqslant 10^6$ the end effect penetrates a distance which is less than 0·6 of the cavity width between the isothermal walls: provided $h_y \geqslant 1{\cdot}2$, there will be some region of the cavity in which the flow is nearly two-dimensional. In a cavity filled with a high Prandtl number fluid, the end effect is purely thermal and is confined to a thin region adjacent to the end walls. The prediction of the numerical solutions is that for high Ra and high Pr the two-dimensional model is adequate provided $h_y > 1$.

Finally, the conclusion reached by Davis (1967), that axial flow in small amplitude convection rolls in finite cavities is negligible, must be regarded as being incorrect for rolls adjacent to a solid boundary. As $Ra \to 0$, the rate of rotation of the cross-sectional flow becomes linearly dependent on Ra. As predicted by Pao, the axial flow for small Re is also linearly dependent on Re and it follows that the end effect depends linearly on Ra. Hence as $Ra \to 0$ the magnitude of the axial flow asymptotes to a constant fraction of the cross-sectional flow. The numerical results presented herein suggest that this fraction will certainly be large enough to ensure that the axial flow is not negligible, especially for $Pr \sim 1$.

The authors are grateful for the assistance of Mr A. D. Graham during the preparation of the diagrams; and for the support provided by a grant from the Australian Research Grants Committee.

REFERENCES

Aziz, K. 1965 Ph.D. thesis, Rice University.
Batchelor, G. K. 1954 *Quart. Appl. Math.* **12**, 209.
Bödewadt, U. T. 1940 *Z. angew. Math. Mech.* **20**, 241.
Boussinesq, J. 1903 *Théorie Analytique de la Chaleur*, vol. 2, p. 172. Gauthier-Villars.
Brooks, R. G. & Probert, S. D. 1972 *J. Mech. Engng Sci.* **14**, 107.
Chorin, A. J. 1968 *Math. Comp.* **22**, 745.
Cormack, D. E., Leal, L. G. & Imberger, J. 1974 *J. Fluid Mech.* **65**, 209.
Cormack, D. E., Leal, L. G. & Seinfeld, J. H. 1974 *J. Fluid Mech.* **65**, 231.
Davis, S. H. 1967 *J. Fluid Mech.* **30**, 465.
Deardorff, J. W. 1970 *J. Fluid Mech.* **41**, 435.
de Vahl Davis, G. 1968 *Int. J. Heat Mass Transfer* **11**, 1675.
de Vahl Davis, G. & Mallinson, G. D. 1975 *J. Fluid Mech.* **72**, 87.
Elder, J. W. 1965*a* *J. Fluid Mech.* **23**, 77.
Elder, J. W. 1965*b* *J. Fluid Mech.* **23**, 99.
Elder, J. W. 1966 *J. Fluid Mech.* **24**, 823.
Fromm, J. E. 1971 *I.B.M. J. Res. Dev.* **15**, 186.
Gershuni, G. Z. 1953 *Zh. Tekh. Fiz.* **23**, 1838.
Gill, A. E. 1966 *J. Fluid Mech.* **26**, 515.
Gill, A. E. & Davey, A. 1969 *J. Fluid Mech.* **35**, 775.
Gill, S. 1951 *Proc. Camb. Phil. Soc.* **47**, 96.
Hart, J. E. 1971 *J. Fluid Mech.* **47**, 547.
Hirasaki, G. J. & Hellums, J. D. 1968 *Quart. Appl. Math.* **16**, 331.
Hirt, C. W. & Cook, J. L. 1972 *J. Comp. Phys.* **10**, 324.
Holst, P. H. & Aziz, K. 1972 *Int. J. Heat Mass Transfer* **15**, 73.
Mallinson, G. D. & de Vahl Davis, G. 1973 *J. Comp. Phys.* **12**, 435.
Pao, H. S. 1970 *J. Appl. Mech.* **37**, 480.
Patanker, S. V., Pratap, V. S. & Spalding, D. B. 1974 *J. Fluid Mech.* **62**, 53.

PATANKER, S. V., PRATAP, V. S. & SPALDING, D. B. 1975 *J. Fluid Mech.* **67**, 58.

PATANKER, S. V. & SPALDING, D. B. 1972 *Int. J. Heat Mass Transfer* **15**, 1787.

POOTS, G. 1958 *Quart. J. Appl. Math.* **11**, 157.

QUON, C. 1972 *Phys. Fluids* **15**, 12.

ROMANELLI, M. J. 1960 In *Mathematical Methods for Digital Computers* (ed. A. Ralston & H. S. Wilf), vol. 2, p. 110. Wiley.

RUBEL, A. & LANDIS, F. 1969 *Phys. Fluids Suppl.* **12**, II 208.

SCHUMANN, U. 1973 Ph.D. dissertation, University of Karlsruhe. (Trans. *N.A.S.A. Tech. Trans.* F15391.)

THOMAS, R. W. & DE VAHL DAVIS, G. 1970 In *Heat Transfer* 1970, vol. 4, paper NC 2.4. Elsevier.

THOMPSON, J. F., SHANKS, S. P. & WU, J. C. 1974 *A.I.A.A. J.* **12**, 787.

TRUESDELL, C. 1954 *The Kinematics of Vorticity.* Bloomington: Indiana University Press.

VEST, C. M. & ARPACI, V. S. 1969 *J. Fluid Mech.* **36**, 1.

WILKES, J. O. & CHURCHILL, S. W. 1966 *A.I.Ch.E. J.* **12**, 161.

WILLIAMS, G. P. 1969 *J. Fluid Mech.* **37**, 727.